Analytical Modeling of the Interaction of a Finite Inducer with a Hidden Long Crack in Ferromagnetic Metals

Mohamad Hossein Ostovarzadeh
Department of Electrical and Computer Engineering, Graduate University of Advanced Technology, Kerman, Iran.
mh.ostovarzadeh@kgut.ac.ir

***Abstract*— This paper proposed a semi-analytical solution for evaluation of field distributions around the surface of a ferromagnetic metallic half space, which contains a hidden long crack and excited by a three-dimensional arbitrary frequency current-carrying inducer. The solution was obtained by using the method of separation of variables in three dimensions. This research assumed that the conductor as a lossy dielectric and used the concept of a rectangular waveguide, which is partially loaded with dielectric to expand all TM and TE field components in the problem. To obtain convergent results, the eigenvalue equation associated with TE modes in the flawed region. By imposing boundary conditions and using the mode matching technique, we obtained a linear system of AX=B was obtained, which is solved to attain the unknown coefficients. The accuracy and efficiency of the modelling technique is confirmed by comparing the results with those obtained by CST finite integration code.**

***Index Terms*— Analytical Modeling; Eddy Currents; Mode Matching; Nondestructive Testing.**

I. INTRODUCTION

The Eddy Current (EC) [1-3] and the Alternating Current Field Measurement (ACFM) techniques [4-7] are among the electromagnetic techniques used for detection and sizing flaws in metals. In these two techniques, a coil is used to induce the eddy currents in the test specimen, and the flaws in the tested specimen result in perturbation of magnetic fields, which can be measured for detection and sizing flaws. In the EC method, the change of the impedance of inducing coil is measured to reveal the metal surface condition, whereas in the ACFM method, the output of a magnetic field sensor attached to the coil is used to monitor metal condition.

The problem of ACFM and EC techniques includes a solution to obtain magnetic fields in the vicinity of a flawed metal excited by a current-carrying inducer. In comparison to the numerical solution methods, the analytical methods are often more efficient because they need relatively fewer computation resources. Therefore, the analytical solution plays an important role in solving the so-called “inverse problem”. In this case, the unknown geometry of a crack is determined iteratively by repetitive calculation of probe output signal for an estimated crack geometry [8]. The analytical solutions also give more insight to the distribution of eddy currents.

In the EC and ACFM testing, we can increase the penetration depth of eddy currents by lowering the exciting frequency. Thus, we can inspect the test specimen at various depths in a single scan by using multi-frequency/pulsed excitation [9-12].

Analytical solutions for arbitrary-frequency excitation are available for flawless metallic slabs [13-15] and cylinders [16-18]. In the case of a flawed workpiece, there are only a few case studies, such as the effect of a long crack in a metallic slab excited by a two-dimensional (2-D) inducer [19] at arbitrary frequency and the problem of a right-angled conductive wedge in the vicinity of a three-dimensional (3-D) coil [20-22].

In our recent works, we solved the problems of field distribution due to a 3D inducer around long cracks in a conductive half space [23-25] and a cylinder [26] analytically. In this work, we extended the problems solved analytically for field distributions around a hidden long crack in a "ferromagnetic" metallic half space excited by a 3D inducer. To model the problem, we assumed the metal as a lossy material with a very large loss tangent. Then, we expanded all TM and TE modes in the flawed workpiece. Then, we changed the eigenvalue equation associated with the TE modes to obtain convergent results.

The paper is organized as follows. In Section II, we briefly present the problem and its formulation where the problem is divided in two: even- and odd-symmetry problems. The solutions for even and odd problems are described in Sections III and IV, respectively. In Section V, the results for field distribution due to a 3-D inducer are predicted and compared with those obtained using a commercial finite integration code.

II. PROBLEM FORMULATION

A schematic of the problem is illustrated in Figure 1. A ferrous conductive half space test specimen with constant conductivity σ, relative permeability μ_r and constant dielectric ε contains a hidden long crack of width g at the depth d. The crack consists of two faces, which are perpendicular to the surface of the test specimen, lying in the direction of the x-axis. The surface of the test specimen is interrogated by the field of an inducer consisting of an arbitrary-shape current-carrying wire. The inducer carries an alternating current of arbitrary frequency f and magnitude I.

To solve the problem posed above, we recognize three regions, namely region I (outside the metal in air), region II (above the long crack in the metal) and region III (inside the metal including the crack). The solution of the problem is similar to the problem of a hidden long crack in a nonmagnetic metallic half space [25]. Therefore, we follow the solution technique described in [25], except in metallic regions, in which the term μ_0 must be replaced to $\mu_0\mu_r$.

For simplicity, we split the solution into two even and odd solutions with respect to the *y*- direction [19, 23-25], which are described in the following section.

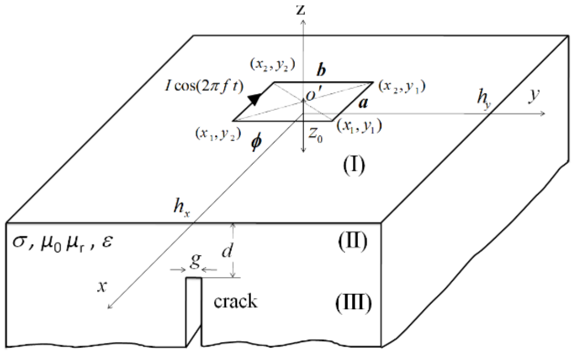

Figure 1: A rectangular inducer above a ferrous half space with a hidden long crack

A. Even Symmetry Solution

As described in [25], we have a potential function ϕ with Laplacian distribution in region I. By truncating the solution at a large distance from the inducer such as h_x and h_y in the *x*- and *y*- directions, respectively, the expression for ϕ in region I is derived as follows:

$$\phi(x,y,z)=\sum_{m=1}^{\infty}\cos(\alpha_m x)\sum_{n=1}^{\infty}\cos(\beta_n y)\times(C_{mn}^{(i)}e^{k_{mn}z}+D_{mn}^{(p)}e^{-k_{mn}z})\qquad(1)$$
$$0\le x\le h_x,\ 0\le y\le h_y\ \ ,0\le z\le z_0$$

where: $k_{mn}^2=\alpha_m^2+\beta_n^2$
m = Mode numbers
n = Mode numbers
α_m = Space frequencies in *x* direction
β_n = Space frequencies in *y* direction

Both α_m and β_n are selected such that the tangential components of $\vec{H}$ become zero at a large distance from the inducer. Hence, $\alpha_m=(2m-1)\pi/(2h_x)$ and $\beta_n=(2n-1)\pi/(2h_y)$. The coefficients C and D are the amplitude of even incident, and they are reflected fields in region I.

Using equations (5) and (6) in [25] and replacing μ_0 with $\mu_0\mu_r$, the expressions for A_y and F_y in region II are derived as:

$$\begin{aligned}&A_y^c=\sum_{m=1}^{\infty}\mu_0\mu_r\sin(\alpha_m x)\cos(\beta_n y)\times(C_{mn}^{(a\_c)}e^{\lambda_{mn}z}-D_{mn}^{(a\_c)}e^{-\lambda_{mn}(z+d)})\\&\lambda_{mn}=\sqrt{\alpha_m^2+\beta_n^2+i\omega\mu_0\mu_r(\sigma+i\omega\varepsilon)}\\&0\le x\le h_x,\ 0<y<h_y\ \ ,-d\le z\le 0\end{aligned}\qquad(2)$$

$$\begin{aligned}&F_y^c=\sum_{m=1}^{\infty}-\varepsilon^*\cos(\alpha_m x)\sin(\beta_n y)\times(C_{mn}^{(f\_c)}e^{\lambda_{mn}z}+D_{mn}^{(f\_c)}e^{-\lambda_{mn}(z+d)})\\&\lambda_{mn}=\sqrt{\alpha_m^2+\beta_n^2+i\omega\mu_0\mu_r(\sigma+i\omega\varepsilon)}\\&0\le x\le h_x,\ 0<y<h_y\ \ ,-d\le z\le 0\end{aligned}\qquad(3)$$

Similarly, one can use (9) and (10) in [25] and replace μ_0 with $\mu_0\mu_r$ for the metallic parts of region III to derive the expressions for the components of A_y and F_y, respectively, as follows:

$$\begin{aligned}&A_y=\sum_{m=1}^{\infty}\mu_0\sin(\alpha_m x)\sum_{n=1}^{\infty}\frac{\cos(p_n y)}{\mu_r a_n\sin(q_n(h_y-y))}C_{mn}^{(a)}e^{\gamma_{mn}(z+d)}\\&q_n=\sqrt{p_n{}^2-k^2-i\omega\mu_0\mu_r(\sigma+i\omega\varepsilon)}\\&\gamma_{mn}=\sqrt{\alpha_m^2+p_n^2-k^2}\\&0\le x\le h_x,\ \begin{matrix}0<y<c\\c<y<h_y\end{matrix}\ ,\ z\le -d\end{aligned}\qquad(4)$$

$$\begin{aligned}&F_y=\sum_{m=1}^{\infty}\cos(\alpha_m x)\sum_{n=1}^{\infty}\frac{-\varepsilon_0\sin(r_n y)}{-\varepsilon^* b_n\cos(s_n(h_y-y))}C_{mn}^{(f)}e^{\zeta_{mn}(z+d)}\\&s_n=\sqrt{r_n{}^2-k^2-i\omega\mu_0\mu_r(\sigma+i\omega\varepsilon)}\\&\zeta_{mn}=\sqrt{\alpha_m^2+r_n{}^2-k^2}\\&0\le x\le h_x,\ \begin{matrix}0\le y\le c\\c\le y\le h_y\end{matrix}\ ,z\le -d\end{aligned}\qquad(5)$$

where: $c=g/2$
$k^2=\omega^2\mu_0\varepsilon_0\ll i\omega\mu_0\mu_r\sigma$ and α_m^2

The eigenvalues associated with TM modes are obtained as described in [25]. However, for the TE modes, we have:

$$b_n=\frac{\sin(r_n c)}{\cos(s_n(h_y-c))}\qquad(6)$$

$$r_n\cot(r_n c)-\frac{s_n}{\mu_r}\tan(s_n(h_y-c))=0\qquad(7)$$

Solving equation (7) leads to large values for r_n and s_n which leads to divergent results. To have appropriate eigenvalues for TE modes, we change equation (7) to the following equation:

$$r_n\cot(s_n(h_y-c))-\frac{s_n}{\mu_r}\tan(r_n c)=0\qquad(8)$$

wherein (8) is solved iteratively for values of s_n by the Newton-Raphson method [19]. The expressions for *y*-component of $\vec{A}'$ are derived as follow [21]:

$$\begin{aligned}&A_y'=\sum_{m=1}^{\infty}\mu_0\sin(\alpha_m x)\sum_{n=1}^{\infty}\frac{a_n'\cos(p_n' y)}{\mu_r\sin(q_n'(h_y-y))}C_{mn}'^{(a)}e^{\gamma_{mn}'(z+d)}\\&p_n'=\sqrt{q_n'^2-k^2-i\omega\mu_0\mu_r(\sigma+i\omega\varepsilon)}\\&\gamma_{mn}'=\sqrt{\alpha_m^2+p_n'^2-k^2}\\&0\le x\le h_x,\ \begin{matrix}0\le y\le c\\c\le y\le h_y\end{matrix}\ ,z\le -d\end{aligned}\qquad(9)$$

where: $q_n'=n\pi/(h_y-c)$
$a_n'=0$

To obtain field perturbation coefficients D_{mn}^p, we match the magnetic field components at the interfaces $z=0$ and $z=-d$, whereas the field component H_x is matched at interface $z=-d$ twice. Further, the field component E_x is to be matched at $z=-d$ [27].

Applying the continuity of H_x, H_y and B_z fields at the interfaces $z=0$ and $z=-d$ and using mode-matching technique [21]respectively, it gives:

$$\begin{aligned}&\alpha_m(\boldsymbol{C}_m^{(\mathrm{i})}+\boldsymbol{D}_m^{(\mathrm{p})})=\\&\boldsymbol{\lambda}_m(\boldsymbol{C}_m^{(\mathrm{a\_c})}+e^{-\boldsymbol{\lambda}_m d}\boldsymbol{D}_m^{(\mathrm{a\_c})})+\frac{\mathrm{i}\alpha_m}{\omega\mu_0\mu_r}\boldsymbol{\beta}(\boldsymbol{C}_m^{(\mathrm{f\_c})}+e^{-\boldsymbol{\lambda}_m d}\boldsymbol{D}_m^{(\mathrm{f\_c})})\end{aligned}\tag{10}$$

$$\begin{aligned}&\frac{h_y}{2}\boldsymbol{\lambda}_m(e^{-\boldsymbol{\lambda}_m d}\boldsymbol{C}_m^{(\mathrm{a\_c})}+\boldsymbol{D}_m^{(\mathrm{a\_c})})\\&\quad+\frac{\mathrm{i}}{\omega\mu_0\mu_r}\frac{h_y}{2}\alpha_m\boldsymbol{\beta}(e^{-\boldsymbol{\lambda}_m d}\boldsymbol{C}_m^{(\mathrm{f\_c})}+D_m^{(\mathrm{f\_c})})\\&\qquad=\boldsymbol{M}_{\mathrm{a}}\boldsymbol{\gamma}_m\boldsymbol{C}_m^{(\mathrm{a})}+\boldsymbol{M}_{\mathrm{b}}\boldsymbol{\gamma}'_m\boldsymbol{C}'^{(\mathrm{a})}_m+\alpha_m\boldsymbol{M}_{\mathrm{c}}\boldsymbol{C}_m^{(\mathrm{f})}\end{aligned}\tag{11}$$

$$\begin{aligned}&\boldsymbol{\beta}(\boldsymbol{C}_m^{(\mathrm{i})}+\boldsymbol{D}_m^{(\mathrm{p})})\\&=\frac{\mathrm{i}}{\omega\mu_0\mu_r}(\boldsymbol{\beta}^2+\mathrm{i}\omega\mu_0\mu_r(\sigma+\mathrm{i}\omega\varepsilon)\times\mathbf{I})(\boldsymbol{C}_m^{(\mathrm{f\_c})}+e^{-\boldsymbol{\lambda}_m d}\boldsymbol{D}_m^{(\mathrm{f\_c})})\end{aligned}\tag{12}$$

$$\begin{aligned}&\frac{h_y}{2\mu_r}(\boldsymbol{\beta}^2+\mathrm{i}\omega\mu_0\mu_r(\sigma+\mathrm{i}\omega\varepsilon)\times\mathbf{I})\times(e^{-\boldsymbol{\lambda}_m d}\boldsymbol{C}_m^{(\mathrm{f\_c})}+\boldsymbol{D}_m^{(\mathrm{f\_c})})\\&\quad=\boldsymbol{M}_{\mathbf{d}}\boldsymbol{C}_m^{(\mathbf{f})}\end{aligned}\tag{13}$$

$$\begin{aligned}\boldsymbol{k}_m(\boldsymbol{C}_m^{(\mathrm{i})}-\boldsymbol{D}_m^{(\mathrm{p})})&=\mu_r\alpha_m(\boldsymbol{C}_m^{(\mathrm{a\_c})}-e^{-\boldsymbol{\lambda}_m d}\boldsymbol{D}_m^{(\mathrm{a\_c})})\\&\quad+\frac{\mathrm{i}}{\omega\mu_0}\boldsymbol{\beta}\boldsymbol{\lambda}_m(\boldsymbol{C}_m^{(\mathrm{f\_c})}-e^{-\boldsymbol{\lambda}_m d}\boldsymbol{D}_m^{(\mathrm{f\_c})})\end{aligned}\tag{14}$$

$$\begin{aligned}&\frac{h_y}{2}\mu_r\alpha_m(e^{-\boldsymbol{\lambda}_m d}\boldsymbol{C}_m^{(\mathrm{a\_c})}-\boldsymbol{D}_m^{(\mathrm{a\_c})})\\&\quad+\frac{\mathrm{i}}{\omega\mu_0}\frac{h_y}{2}\boldsymbol{\beta}\boldsymbol{\lambda}_m(e^{-\boldsymbol{\lambda}_m d}\boldsymbol{C}_m^{(\mathrm{f\_c})}-\boldsymbol{D}_m^{(\mathrm{f\_c})})\\&=\alpha_m\boldsymbol{M}'_{\mathrm{a}}\boldsymbol{C}_m^{(\mathrm{a})}+\alpha_m\mu_r\boldsymbol{M}_{\mathrm{b}}\boldsymbol{C}'^{(\mathrm{a})}_m+\boldsymbol{M}'_{\mathrm{c}}\boldsymbol{\zeta}_m\boldsymbol{C}_m^{(\mathrm{f})}\end{aligned}\tag{15}$$

where: $\boldsymbol{C}_m$ = Column vector
$\boldsymbol{D}_m$ = Column vector

Both $\boldsymbol{C}_m$ and $\boldsymbol{D}_m$ have expansion coefficients for a particular value of α_m, which is limited to N_y components. The λ_{mn}, β_n, γ_{mn} , γ'_{mn}, k_{mn} and ζ_{mn} have been formed into $N_y \times N_y$ diagonal matrices $\boldsymbol{\lambda}_m, \boldsymbol{\beta}, \boldsymbol{\gamma}_m , \boldsymbol{\gamma}'_m, \boldsymbol{k}_m$ and $\boldsymbol{\zeta}_m$, respectively, based on the following equation:

$$\begin{aligned}\boldsymbol{M}_{\mathrm{c}}[n,n']=\frac{\mathrm{i}}{\omega\mu_0}&(r_{n'}\int_0^c\cos(\beta_n y)\cos(r_{n'}y)dy\\&+\frac{b_{n'}s_{n'}}{\mu_r}\int_c^{h_y}\cos(\beta_n y)\sin(s_{n'}(h_y-y))dy)\end{aligned}\tag{16}$$

$$\begin{aligned}\boldsymbol{M}_{\mathrm{d}}[n,n']=(r_{n'}^2-k^2)(&\int_0^c\sin(\beta_n y)\sin(r_{n'}y)dy\\&+\frac{b_{n'}}{\mu_r}\int_c^{h_y}\sin(\beta_n y)\cos(s_{n'}(h_y-y))dy\ )\end{aligned}\tag{17}$$

$$\begin{aligned}\boldsymbol{M}'_{\mathrm{a}}[n,n']=(&\int_0^c\cos(\beta_n y)\cos(p_{n'}y)dy\\&+\mu_r a_{n'}\int_c^{h_y}\cos(\beta_n y)\sin(q_{n'}(h_y-y))dy)\end{aligned}\tag{18}$$

$$\begin{aligned}\boldsymbol{M}'_{\mathrm{c}}[n,n']=\frac{\mathrm{i}}{\omega\mu_0}(&r_{n'}\int_0^c\cos(\beta_n y)\cos(r_{n'}y)dy\\&+b_{n'}s_{n'}\int_c^{h_y}\cos(\beta_n y)\sin(s_{n'}(h_y-y))dy)\end{aligned}\tag{19}$$

By first matching H_x field at the crack's mouth and using mode-matching technique, we derive:

$$\begin{aligned}&\boldsymbol{c}\,\boldsymbol{\gamma}_m\boldsymbol{C}_m^{(\mathrm{a})}+\alpha_m\boldsymbol{M}_{\mathrm{e}}\boldsymbol{C}_m^{(\mathrm{f})}\\&\quad=\boldsymbol{M}_{\mathrm{f}}\boldsymbol{\lambda}_m(e^{-\boldsymbol{\lambda}_m d}\boldsymbol{C}_m^{(\mathrm{a\_c})}+\boldsymbol{D}_m^{(\mathrm{a\_c})})\\&\qquad+\frac{\mathrm{i}\alpha_m}{\omega\mu_0}\boldsymbol{M}_{\mathrm{f}}\boldsymbol{\beta}(e^{-\boldsymbol{\lambda}_m d}\boldsymbol{C}_m^{(\mathrm{f\_c})}+\boldsymbol{D}_m^{(\mathrm{f\_c})})\end{aligned}\tag{20}$$

Applying the continuity of E_x at the interface $z = -d$and using the mode-matching technique [21] gives:

$$\begin{aligned}&\frac{h_y}{2}\frac{\alpha_m\boldsymbol{\beta}}{\sigma+\mathrm{i}\omega\varepsilon}(e^{-\boldsymbol{\lambda}_m d}\boldsymbol{C}_m^{(\mathrm{a\_c})}-\boldsymbol{D}_m^{(\mathrm{a\_c})})\\&\quad+\frac{h_y}{2}\boldsymbol{\lambda}_m(e^{-\boldsymbol{\lambda}_m d}\boldsymbol{C}_m^{(\mathrm{f\_c})}-\boldsymbol{D}_m^{(\mathrm{f\_c})})\\&=\alpha_m\boldsymbol{M}_{\mathrm{g}}\boldsymbol{C}_m^{(\mathrm{a})}+\alpha_m\boldsymbol{M}_{\mathrm{h}}\boldsymbol{C}'^{(\mathrm{a})}_m+\boldsymbol{M}_{\mathrm{i}}\boldsymbol{\zeta}_m\boldsymbol{C}_m^{(\mathrm{f})}\end{aligned}\tag{21}$$

Matrices $\boldsymbol{M}_{\mathrm{a}}$, $\boldsymbol{M}_{\mathrm{b}}$, $\boldsymbol{c}$, $\boldsymbol{M}_{\mathrm{e}}$, $\boldsymbol{M}_{\mathrm{f}}$, $\boldsymbol{M}_{\mathrm{g}}$, $\boldsymbol{M}_{\mathrm{h}}$ and $\boldsymbol{M}_{\mathrm{i}}$ are given in [25]. The unknown coefficients in (10)-(15) and (20)-(21) can be derived as in equation (22). The matrix inversion is performed for all values of α_m.

$$\begin{bmatrix}\boldsymbol{D}_m^{(\mathrm{p})}\\\boldsymbol{C}_m^{(\mathrm{a_c})}\\\boldsymbol{D}_m^{(\mathrm{a_c})}\\\boldsymbol{C}_m^{(\mathrm{f_c})}\\\boldsymbol{D}_m^{(\mathrm{f_c})}\\\boldsymbol{C}_m^{(\mathrm{a})}\\\boldsymbol{C}'^{(\mathrm{a})}_m\\\boldsymbol{C}_m^{(\mathrm{f})}\end{bmatrix}=\begin{bmatrix}\boldsymbol{\alpha}_m & -\boldsymbol{\lambda}_m & -\boldsymbol{\lambda}_m e^{-\boldsymbol{\lambda}_m d} & -\frac{\mathrm{i}\alpha_m}{\omega\mu_0\mu_r}\boldsymbol{\beta} & -\frac{\mathrm{i}\alpha_m}{\omega\mu_0\mu_r}\boldsymbol{\beta}e^{-\boldsymbol{\lambda}_m d} & \mathbf{0} & \mathbf{0} & \mathbf{0}\\
\boldsymbol{k}_m & \mu_r\boldsymbol{\alpha}_m & -\mu_r\alpha_m e^{-\boldsymbol{\lambda}_m d} & \frac{\mathrm{i}}{\omega\mu_0}\boldsymbol{\lambda}_m\boldsymbol{\beta} & -\frac{\mathrm{i}}{\omega\mu_0}\boldsymbol{\lambda}_m\boldsymbol{\beta}e^{-\boldsymbol{\lambda}_m d} & \mathbf{0} & \mathbf{0} & \mathbf{0}\\
\mathbf{0} & \frac{h_y}{2}\frac{\alpha_m\boldsymbol{\beta}}{\sigma+\mathrm{i}\omega\varepsilon}e^{-\boldsymbol{\lambda}_m d} & -\frac{h_y}{2}\frac{\alpha_m\boldsymbol{\beta}}{\sigma+\mathrm{i}\omega\varepsilon} & \frac{h_y}{2}\boldsymbol{\lambda}_m e^{-\boldsymbol{\lambda}_m d} & -\frac{h_y}{2}\boldsymbol{\lambda}_m & -\alpha_m\boldsymbol{M}_{\mathrm{g}} & -\alpha_m\boldsymbol{M}_{\mathrm{h}} & -\boldsymbol{M}_{\mathrm{i}}\boldsymbol{\zeta}_m\\
-\boldsymbol{\beta} & \mathbf{0} & \mathbf{0} & \frac{\mathrm{i}}{\omega\mu_0\mu_r}(\boldsymbol{\beta}^2+\mathrm{i}\omega\mu_0\mu_r(\sigma+\mathrm{i}\omega\varepsilon)\times\mathbf{I}) & \frac{\mathrm{i}}{\omega\mu_0\mu_r}(\boldsymbol{\beta}^2+\mathrm{i}\omega\mu_0\mu_r(\sigma+\mathrm{i}\omega\varepsilon)\times\mathbf{I})e^{-\boldsymbol{\lambda}_m d} & \mathbf{0} & \mathbf{0} & \mathbf{0}\\
\mathbf{0} & \frac{h_y}{2}\boldsymbol{\lambda}_m e^{-\boldsymbol{\lambda}_m d} & \frac{h_y}{2}\boldsymbol{\lambda}_m & \frac{\mathrm{i}\alpha_m}{\omega\mu_0\mu_r}\frac{h_y}{2}\boldsymbol{\beta}e^{-\boldsymbol{\lambda}_m d} & \frac{\mathrm{i}\alpha_m}{\omega\mu_0\mu_r}\frac{h_y}{2}\boldsymbol{\beta} & -\boldsymbol{M}_{\mathrm{a}}\boldsymbol{\gamma}_m & -\boldsymbol{M}_{\mathrm{b}}\boldsymbol{\gamma}'_m & -\alpha_m\boldsymbol{M}_{\mathrm{c}}\\
\mathbf{0} & -\boldsymbol{M}_{\mathrm{f}}\boldsymbol{\lambda}_m e^{-\boldsymbol{\lambda}_m d} & -\boldsymbol{M}_{\mathrm{f}}\boldsymbol{\lambda}_m & -\frac{\mathrm{i}\alpha_m}{\omega\mu_0}\boldsymbol{M}_{\mathrm{f}}\boldsymbol{\beta}e^{-\boldsymbol{\lambda}_m d} & -\frac{\mathrm{i}\alpha_m}{\omega\mu_0}\boldsymbol{M}_{\mathrm{f}}\boldsymbol{\beta} & \mathbf{c}\boldsymbol{\gamma}_m & \mathbf{0} & \alpha_m\boldsymbol{M}_{\mathrm{e}}\\
\mathbf{0} & -\frac{h_y}{2}\mu_r\alpha_m e^{-\boldsymbol{\lambda}_m d} & \frac{h_y}{2}\mu_r\boldsymbol{\alpha}_m & -\frac{\mathrm{i}}{\omega\mu_0}\frac{h_y}{2}\boldsymbol{\beta}\boldsymbol{\lambda}_m e^{-\boldsymbol{\lambda}_m d} & \frac{\mathrm{i}}{\omega\mu_0}\frac{h_y}{2}\boldsymbol{\beta}\boldsymbol{\lambda}_m & \alpha_m\boldsymbol{M}'_{\mathrm{a}} & \alpha_m\mu_r\boldsymbol{M}_{\mathrm{b}} & \boldsymbol{M}'_{\mathrm{c}}\boldsymbol{\zeta}_m\\
\mathbf{0} & \mathbf{0} & \mathbf{0} & -\frac{h_y}{2\mu_r}(\boldsymbol{\beta}^2+\mathrm{i}\omega\mu_0\mu_r(\sigma+\mathrm{i}\omega\varepsilon)\times\mathbf{I})e^{-\boldsymbol{\lambda}_m d} & -\frac{h_y}{2\mu_r}(\boldsymbol{\beta}^2+\mathrm{i}\omega\mu_0\mu_r(\sigma+\mathrm{i}\omega\varepsilon)\times\mathbf{I}) & \mathbf{0} & \mathbf{0} & \boldsymbol{M}_{\mathrm{d}}\end{bmatrix}^{-1}\begin{bmatrix}-\alpha_m\boldsymbol{C}_m^{(\mathrm{i})}\\\boldsymbol{k}_m\boldsymbol{C}_m^{(\mathrm{i})}\\\mathbf{0}\\\boldsymbol{\beta}\boldsymbol{C}_m^{(\mathrm{i})}\\\mathbf{0}\\\mathbf{0}\\\mathbf{0}\\\mathbf{0}\end{bmatrix}\tag{22}$$

where: $\boldsymbol{\alpha}_m$ = Diagonal matrix whose diagonal elements are α_m (m = 1, 2, … N_x)
N_x = Truncation limit.

B. Odd Symmetry Solution

The expression for the odd component of ϕ in region I is as follows [25]:

$$\phi(x,y,z)=\sum_{m=1}^{\infty}\cos(\alpha_m x)\sum_{n=1}^{\infty}\sin(\beta_n y)(C_{mn}^{(i)}e^{k_{mn}z}+D_{mn}^{(p)}e^{-k_{mn}z})$$
$$0\le x\le h_x,\ 0\le y\le h_y\ \ ,0\le z\le z_0 \tag{23}$$

Where: $\alpha_m=(2m-1)\pi/(2h_x)$
$\beta_n=n\pi/h_y$

Using equations (5) and (6) in [25] and replacing μ_0 with $\mu_0\mu_r$, the expressions for A_y and F_y in region II are obtained as follows:

$$A_y^c=\sum_{m=1}^{\infty}\mu_0\mu_r\sin(\alpha_m x)\sin(\beta_n y)\times(C_{mn}^{(a\_c)}e^{\lambda_{mn}z}-D_{mn}^{(a\_c)}e^{-\lambda_{mn}(z+d)})$$
$$\lambda_{mn}=\sqrt{\alpha_m^2+\beta_n^2+\mathrm{i}\omega\mu_0\mu_r(\sigma+\mathrm{i}\omega\varepsilon)}$$
$$0\le x\le h_x,\ 0<y<h_y\ \ ,-d\le z\le 0 \tag{24}$$

$$F_y^c=\sum_{m=1}^{\infty}-\varepsilon^*\cos(\alpha_m x)\cos(\beta_n y)\times(C_{mn}^{(f\_c)}e^{\lambda_{mn}z}+D_{mn}^{(f\_c)}e^{-\lambda_{mn}(z+d)})$$
$$\lambda_{mn}=\sqrt{\alpha_m^2+\beta_n^2+\mathrm{i}\omega\mu_0\mu_r(\sigma+\mathrm{i}\omega\varepsilon)}$$
$$0\le x\le h_x,\ 0<y<h_y\ \ ,-d\le z\le 0 \tag{25}$$

Similarly, one can use (9) and (10) in [25] and replace μ_0 with $\mu_0\mu_r$ for the metallic parts of region III to derive the expressions for the components of A_y and F_y, in region III as follows:

$$A_y=\sum_{m=1}^{\infty}\mu_0\sin(\alpha_m x)\sum_{n=1}^{\infty}\frac{\sin(p_n y)}{\mu_r a_n\sin(q_n(h_y-y))}C_{mn}^{(a)}e^{\gamma_{mn}(z+d)}$$
$$q_n=\sqrt{p_n{}^2-k^2-\mathrm{i}\omega\mu_0\mu_r(\sigma+\mathrm{i}\omega\varepsilon)}$$
$$\gamma_{mn}=\sqrt{\alpha_m^2+p_n^2-k^2}$$
$$0\le x\le h_x,\ \begin{matrix}0<y<c\\ c<y<h_y\end{matrix}\ ,z\le -d \tag{26}$$

$$F_y=\sum_{m=1}^{\infty}\cos(\alpha_m x)\sum_{n=1}^{\infty}\frac{-\varepsilon_0\cos(r_n y)}{-\varepsilon^* b_n\cos(s_n(h_y-y))}C_{mn}^{(f)}e^{\zeta_{mn}(z+d)}$$
$$s_n=\sqrt{r_n{}^2-k^2-\mathrm{i}\omega\mu_0\mu_r(\sigma+\mathrm{i}\omega\varepsilon)}$$
$$\zeta_{mn}=\sqrt{\alpha_m^2+r_n{}^2-k^2}$$
$$0\le x\le h_x,\ \begin{matrix}0\le y\le c\\ c\le y\le h_y\end{matrix}\ ,z\le -d \tag{27}$$

As discussed in [25], the TM mode associated with eigenvalues p_n and q_n has an insignificant value. For TE modes we have:

$$b_n=\frac{\cos(r_n c)}{\cos(s_n(h_y-c))} \tag{28}$$

$$r_n\tan(r_n c)+\frac{s_n}{\mu_r}\tan(s_n(h_y-c))=0 \tag{29}$$

Where we change equation (29) to the following equation, and solve equation (30) for values of s_n using Newton-Raphson method [19].

$$r_n\cot(s_n(h_y-c))+\frac{s_n}{\mu_r}\cot(r_n c)=0 \tag{30}$$

The expressions for y-component of $\vec{A}'$ are derived as follow [21]:

$$A'_y=\sum_{m=1}^{\infty}\mu_0\sin(\alpha_m x)\sum_{n=1}^{\infty}\frac{a'_n\sin(p'_n y)}{\mu_r\sin(q'_n(h_y-y))}C_{mn}^{\prime(a)}e^{\gamma'_{mn}(z+d)}$$
$$q'_n=\sqrt{p_n'^2-k^2-\mathrm{i}\omega\mu_0\mu_r(\sigma+\mathrm{i}\omega\varepsilon)}$$
$$\gamma'_{mn}=\sqrt{\alpha_m^2+p_n'^2-k^2}$$
$$0\le x\le h_x,\ \begin{matrix}0<y<c\\ c<y<h_y\end{matrix}\ ,z\le -d \tag{31}$$

where: $q'_n=n\pi/(h_y-c)$
$a'_n=0$

To obtain field perturbation coefficient $D_{mn}^{(p)}$, the magnetic field components H_x, H_y and B_z are matched at interfaces $z=0$ and $z=-d$. Also the field component E_x is to be matched at the interface $z=-d$.

Applying the continuity of H_x, H_y and B_Z fields at $z=0$ and $z=-d$, respectively, the followings are derived:

$$\alpha_m(\boldsymbol{C}_m^{(i)}+\boldsymbol{D}_m^{(p)})=\boldsymbol{\lambda}_m(\boldsymbol{C}_m^{(a\_c)}+e^{-\boldsymbol{\lambda}_m d}\boldsymbol{D}_m^{(a\_c)})-\frac{\mathrm{i}\alpha_m}{\omega\mu_0\mu_r}\boldsymbol{\beta}(\boldsymbol{C}_m^{(f\_c)}+e^{-\boldsymbol{\lambda}_m d}\boldsymbol{D}_m^{(f\_c)}) \tag{32}$$

$$\frac{h_y}{2}\boldsymbol{\lambda}_m(e^{-\boldsymbol{\lambda}_m d}\boldsymbol{C}_m^{(a\_c)}+\boldsymbol{D}_m^{(a\_c)})-\frac{\mathrm{i}}{\omega\mu_0\mu_r}\frac{h_y}{2}\alpha_m\boldsymbol{\beta}(e^{-\boldsymbol{\lambda}_m d}\boldsymbol{C}_m^{(f\_c)}+D_m^{(f\_c)})=\boldsymbol{M}_b\boldsymbol{\gamma}'_m\boldsymbol{C}_m^{\prime(a)}+\alpha_m\boldsymbol{M}_c\boldsymbol{C}_m^{(f)} \tag{33}$$

$$\boldsymbol{\beta}(\boldsymbol{C}_m^{(i)}+\boldsymbol{D}_m^{(p)})=\frac{-\mathrm{i}}{\omega\mu_0\mu_r}(\boldsymbol{\beta}^2+\mathrm{i}\omega\mu_0\mu_r(\sigma+\mathrm{i}\omega\varepsilon)\times\mathbf{I})(\boldsymbol{C}_m^{(f\_c)}+e^{-\boldsymbol{\lambda}_m d}\boldsymbol{D}_m^{(f\_c)}) \tag{34}$$

$$\frac{h_y}{2\mu_r}(\boldsymbol{\beta}^2+\mathrm{i}\omega\mu_0\mu_r(\sigma+\mathrm{i}\omega\varepsilon)\times\mathbf{I})\times(e^{-\boldsymbol{\lambda}_m d}\boldsymbol{C}_m^{(f\_c)}+\boldsymbol{D}_m^{(f\_c)})=\boldsymbol{M}_d\boldsymbol{C}_m^{(f)} \tag{35}$$

$$\boldsymbol{k}_m(\boldsymbol{C}_m^{(i)}-\boldsymbol{D}_m^{(p)})=\mu_r\alpha_m(\boldsymbol{C}_m^{(a\_c)}-e^{-\boldsymbol{\lambda}_m d}\boldsymbol{D}_m^{(a\_c)})-\frac{\mathrm{i}}{\omega\mu_0}\boldsymbol{\beta}\boldsymbol{\lambda}_m(\boldsymbol{C}_m^{(f\_c)}-e^{-\boldsymbol{\lambda}_m d}\boldsymbol{D}_m^{(f\_c)}) \tag{36}$$

$$\frac{h_y}{2}\mu_r\alpha_m(e^{-\boldsymbol{\lambda}_m d}\boldsymbol{C}_m^{(a\_c)}-\boldsymbol{D}_m^{(a\_c)})-\frac{\mathrm{i}}{\omega\mu_0}\frac{h_y}{2}\boldsymbol{\beta}\boldsymbol{\lambda}_m(e^{-\boldsymbol{\lambda}_m d}\boldsymbol{C}_m^{(f\_c)}-\boldsymbol{D}_m^{(f\_c)})=\alpha_m\mu_r\boldsymbol{M}_b\boldsymbol{C}_m^{\prime(a)}+\boldsymbol{M}'_c\boldsymbol{\zeta}_m\boldsymbol{C}_m^{(f)} \tag{37}$$

Where $\boldsymbol{M}_c[n,n']$, $\boldsymbol{M}_d[n,n']$ and $\boldsymbol{M}'_c[n,n']$ are as follows:

$$\boldsymbol{M}_c[n,n']=\frac{1}{\mathrm{i}\omega\mu_0}(r_{n'}\int_0^c\sin(\beta_n y)\sin(r_{n'}y)dy-\frac{b_{n'}s_{n'}}{\mu_r}\int_c^{h_y}\sin(\beta_n y)\sin(s_{n'}(h_y-y))dy)) \tag{38}$$

$$\boldsymbol{M}_{\mathrm{d}}[n,n'] = (r_{n'}^2 - k^2)\Big(\int_0^c \cos(\beta_n y)\cos(r_{n'} y)dy + \frac{b_{n'}}{\mu_r}\int_c^{h_y} \cos(\beta_n y)\cos(s_{n'}(h_y - y))dy\Big) \tag{39}$$

$$\boldsymbol{M}'_{\mathrm{c}}[n,n'] = \frac{1}{\mathrm{i}\omega\mu_0}\Big(r_{n'}\int_0^c \sin(\beta_n y)\sin(r_{n'} y)dy - b_{n'} s_{n'}\int_c^{h_y} \sin(\beta_n y)\sin(s_{n'}(h_y - y))dy\Big) \tag{40}$$

Applying the continuity of E_x at the interface $z = -d$ and using the mode-matching technique result in the following:

$$-\frac{h_y}{2}\frac{\alpha_m \boldsymbol{\beta}}{\sigma + \mathrm{i}\omega\varepsilon}(e^{-\lambda_m d}\boldsymbol{C}_m^{(\mathrm{a\_c})} - \boldsymbol{D}_m^{(\mathrm{a\_c})}) + \frac{h_y}{2}\boldsymbol{\lambda}_m(e^{-\lambda_m d}\boldsymbol{C}_m^{(\mathrm{f\_c})} - \boldsymbol{D}_m^{(\mathrm{f\_c})}) = \alpha_m \boldsymbol{M}_{\mathrm{h}}\boldsymbol{C}_m'^{(\mathrm{a})} + \boldsymbol{M}_{\mathrm{i}}\boldsymbol{\zeta}_m \boldsymbol{C}_m^{(\mathrm{f})} \tag{41}$$

where: $\boldsymbol{M}_{\mathrm{b}}$ = Given in [25]
$\boldsymbol{M}_{\mathrm{h}}$ = Given in [25]
$\boldsymbol{M}_{\mathrm{i}}$ = Given in [25]

The unknown coefficients in (32)-(37) and (41) can be determined using the matrix given in equation (42), where the matrix inversion is performed for all values of α_m.

$$\begin{bmatrix} \boldsymbol{D}_m^{(\mathrm{p})} \\ \boldsymbol{C}_m^{(\mathrm{a\_c})} \\ \boldsymbol{D}_m^{(\mathrm{a\_c})} \\ \boldsymbol{C}_m^{(\mathrm{f\_c})} \\ \boldsymbol{D}_m^{(\mathrm{f\_c})} \\ \boldsymbol{C}_m'^{(\mathrm{a})} \\ \boldsymbol{C}_m^{(\mathrm{f})} \end{bmatrix} = \begin{bmatrix} \boldsymbol{\alpha}_m & -\boldsymbol{\lambda}_m & -\boldsymbol{\lambda}_m e^{-\lambda_m d} & \frac{\mathrm{i}\alpha_m}{\omega\mu_0\mu_r}\boldsymbol{\beta} & \frac{\mathrm{i}\alpha_m}{\omega\mu_0\mu_r}\boldsymbol{\beta}e^{-\lambda_m d} & \mathbf{0} & \mathbf{0} \\ \boldsymbol{k}_m & \mu_r\boldsymbol{\alpha}_m & -\mu_r\alpha_m e^{-\lambda_m d} & \frac{-\mathrm{i}}{\omega\mu_0}\boldsymbol{\lambda}_m\boldsymbol{\beta} & \frac{\mathrm{i}}{\omega\mu_0}\boldsymbol{\lambda}_m\boldsymbol{\beta}e^{-\lambda_m d} & \mathbf{0} & \mathbf{0} \\ \mathbf{0} & -\frac{h_y}{2}\frac{\alpha_m\boldsymbol{\beta}}{\sigma+\mathrm{i}\omega\varepsilon}e^{-\lambda_m d} & \frac{h_y}{2}\frac{\alpha_m\boldsymbol{\beta}}{\sigma+\mathrm{i}\omega\varepsilon} & \frac{h_y}{2}\boldsymbol{\lambda}_m e^{-\lambda_m d} & -\frac{h_y}{2}\boldsymbol{\lambda}_m & -\alpha_m\boldsymbol{M}_{\mathrm{h}} & -\boldsymbol{M}_{\mathrm{i}}\boldsymbol{\zeta}_m \\ -\boldsymbol{\beta} & \mathbf{0} & \mathbf{0} & \frac{-\mathrm{i}}{\omega\mu_0\mu_r}(\boldsymbol{\beta}^2 + \mathrm{i}\omega\mu_0\mu_r(\sigma+\mathrm{i}\omega\varepsilon)\times\mathbf{I}) & \frac{-\mathrm{i}}{\omega\mu_0\mu_r}(\boldsymbol{\beta}^2 + \mathrm{i}\omega\mu_0\mu_r(\sigma+\mathrm{i}\omega\varepsilon)\times\mathbf{I})e^{-\lambda_m d} & \mathbf{0} & \mathbf{0} \\ \mathbf{0} & \frac{h_y}{2}\boldsymbol{\lambda}_m e^{-\lambda_m d} & \frac{h_y}{2}\boldsymbol{\lambda}_m & \frac{-\mathrm{i}\alpha_m}{\omega\mu_0\mu_r}\frac{h_y}{2}\boldsymbol{\beta}e^{-\lambda_m d} & \frac{-\mathrm{i}\alpha_m}{\omega\mu_0\mu_r}\frac{h_y}{2}\boldsymbol{\beta} & -\boldsymbol{M}_{\mathrm{b}}\boldsymbol{\gamma}'_m & -\alpha_m\boldsymbol{M}_{\mathrm{c}} \\ \mathbf{0} & -\frac{h_y}{2}\mu_r\alpha_m e^{-\lambda_m d} & \frac{h_y}{2}\mu_r\boldsymbol{\alpha}_m & \frac{\mathrm{i}}{\omega\mu_0}\frac{h_y}{2}\boldsymbol{\beta}\boldsymbol{\lambda}_m e^{-\lambda_m d} & \frac{-\mathrm{i}}{\omega\mu_0}\frac{h_y}{2}\boldsymbol{\beta}\boldsymbol{\lambda}_m & \alpha_m\mu_r\boldsymbol{M}_{\mathrm{b}} & \boldsymbol{M}'_{\mathrm{c}}\boldsymbol{\zeta}_m \\ \mathbf{0} & \mathbf{0} & \mathbf{0} & -\frac{h_y}{2\mu_r}(\boldsymbol{\beta}^2 + \mathrm{i}\omega\mu_0\mu_r(\sigma+\mathrm{i}\omega\varepsilon)\times\mathbf{I})e^{-\lambda_m d} & -\frac{h_y}{2\mu_r}(\boldsymbol{\beta}^2 + \mathrm{i}\omega\mu_0\mu_r(\sigma+\mathrm{i}\omega\varepsilon)\times\mathbf{I}) & \mathbf{0} & \boldsymbol{M}_{\mathrm{d}} \end{bmatrix}^{-1} \begin{bmatrix} -\alpha_m\boldsymbol{C}_m^{(\mathrm{i})} \\ \boldsymbol{k}_m\boldsymbol{C}_m^{(\mathrm{i})} \\ \mathbf{0} \\ \boldsymbol{\beta}\boldsymbol{C}_m^{(\mathrm{i})} \\ \mathbf{0} \\ \mathbf{0} \\ \mathbf{0} \end{bmatrix} \tag{42}$$

III. RESULTS

To demonstrate the validity of the proposed modelling technique, results of various simulations are presented. Results are associated with a current carrying rectangular inducer above the surface of a steel half space ($\mu_r = 100$ and $\sigma = 6\times10^6$ S/m) containing a hidden long crack with g = 0.4 mm and is excited by an alternating current source of I = 1A. To evaluate the performance of the proposed technique in a general case where both the even- and odd- symmetry solutions exist, the centre of the inducer (point o' in Figure 1) is located at x = 0, y = 2 mm and z_0 = 5 mm.

We present the theoretical and simulation results for a finite rectangular inducer which represents a 3-D problem. With reference to Figure 1, a rectangular inducer with length b = 20 mm and width a =10 mm is located parallel to the y- and x- axis, respectively. To achieve accurate results, the values of h_x and h_y are selected 20 times greater than the exciter dimensions. The values of N_x and N_y are also selected 40 and 200, respectively.

We examine the y-component of magnetic field distributions along the y-axis at a lift-off distance z_s = 0.7 mm. Variations of magnitude and phase of H_y along the scanning path for operating frequencies f = 500 Hz, 1 kHz and 2 kHz when the crack is located at depth d = 1 mm are shown in Figures. 2, 3, and 4, respectively. To validate these results, we have repeated the simulations, using the well-known CST finite integration code [28]. The code has been used in magnetoquasistatic regime with adaptive meshing for 1e^{-4} accuracy. The final number of hexahedral mesh cells is 280500, taking 2minutes for simulation on a 2.83 GHz Quad core CPU with 3.25 GB of RAM. A comparison of the results shown in Figures 2, 3, and 4 confirms the accuracy of the proposed model. The computation time required in the finite integration method is about 1.5 times more than that required in the method described in this paper.

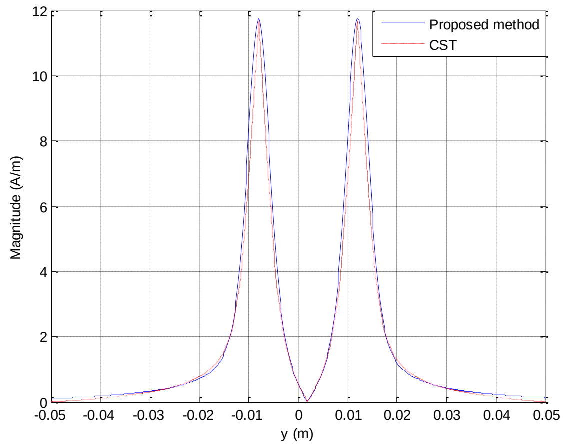

(a)

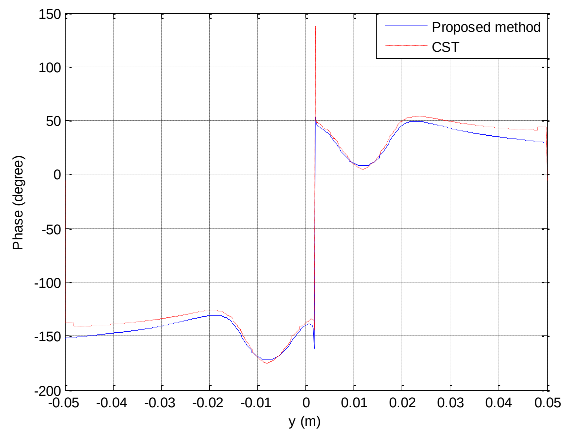

(b)

Figure 2: (a) Magnitude and (b) phase of Hy along the y-axis at a lift-off distance z_s= 0.7 mm below a rectangular inducer with a = 10 mm, b = 20 mm and o' = (0, 2 mm, 5 mm) in Figure 1, when the inducer is located in

air and above steel half space containing a long hidden crack with gap distance g = 0.4 mm at depth 1 mm. For these plots, f = 500 Hz.

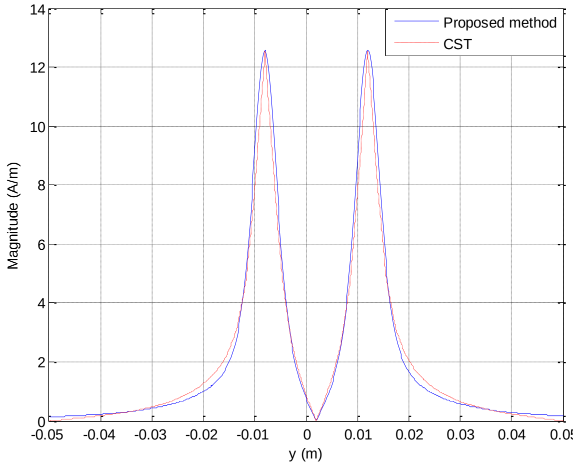

(a)

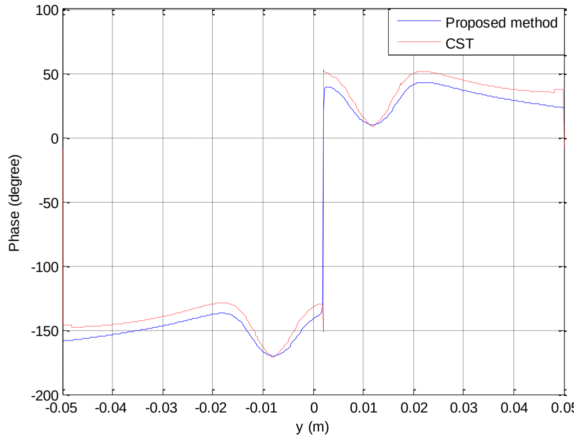

(b)

Figure 3: (a) Magnitude and (b) phase of Hy along the y-axis at a lift-off distance z_s = 0.7 mm below a rectangular inducer with a = 10 mm, b = 20 mm and o' = (0, 2 mm, 5mm) in Figure 1, when the inducer is located in air and above steel half space containing a long-hidden crack with gap distance g = 0.4 mm at depth 1 mm. For these plots, f = 1 kHz.

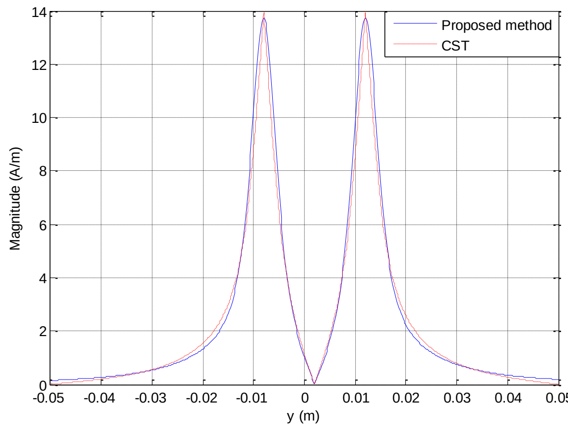

(a)

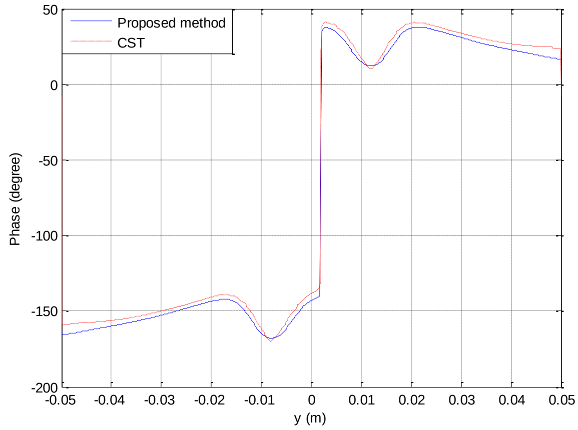

(b)

Figure 4: (a) Magnitude and (b) phase of H_y along the y-axis at a lift-off distance z_s= 0.7 mm below a rectangular inducer with a = 10 mm, b = 20 mm and o' = (0, 2 mm, 5 mm) in Figure 1, when the inducer is located in air and above steel half space containing a hidden long crack with gap distance g = 0.4 mm at depth 1 mm. For these plots, For these plots, f = 2 kHz.

In the next set of simulations, we study the effect of frequency on the sensitivity of crack detection. In these simulations, the crack is assumed to be at depth d = 1 mm while the exciting frequency varies. Variations of magnitude and phase of crack signals for operating frequencies f = 500Hz, 1 kHz and 2 kHz are shown in Figure 5. The crack signal is obtained by subtracting the fields of ferrous half space [13-15] from that of flawed ferrous half space. The study of crack signals in this figure clearly demonstrates that the magnitude of crack signal tends to decrease as the exciting frequency increases.

Finally, we study the effect of crack depth on the sensitivity of crack detection. In the simulations carried out, the frequency is assumed to be f = 1 kHz, while the crack depth takes various values. Variations of magnitude and phase of crack signals for cracks at depths d = 1 mm, 2mm and 3mm are shown in Figure 6. A comparison of the results in Figure 6 demonstrates that for a given operating frequency, the magnitude of crack signal tends to decrease severely as it is located deeper in the metal.

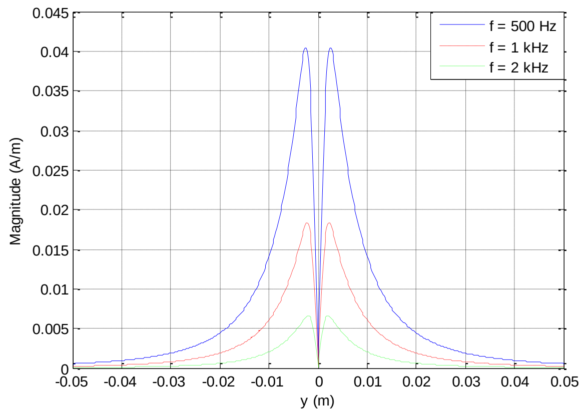

(a)

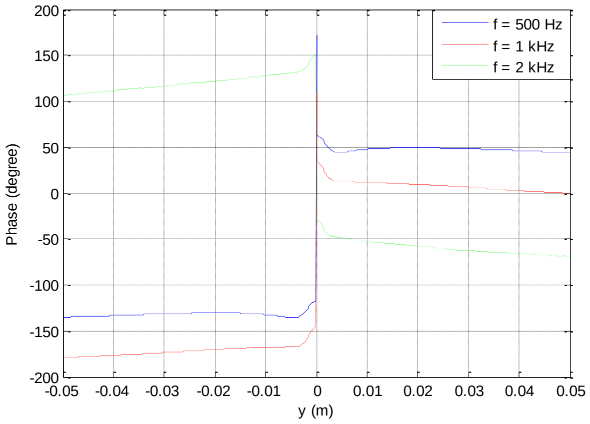

(b)

Figure 5: (a) Magnitude and (b) phase of crack signal ($H_{y,c}$) along the *y*-axis at a lift-off distance z_s = 0.7 mm below a rectangular inducer with a = 10 mm, *b* = 20 mm and *o′* = (0, 2 mm, 5 mm) in Figure 1, when the inducer is located in air and above steel half space containing a long hidden crack with gap distance *g* = 0.4 mm at depth 1 mm.

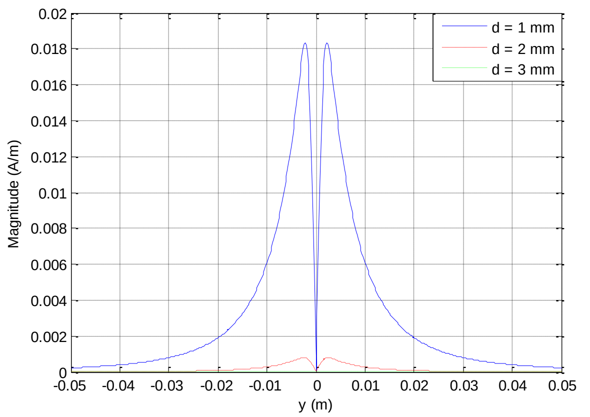

(a)

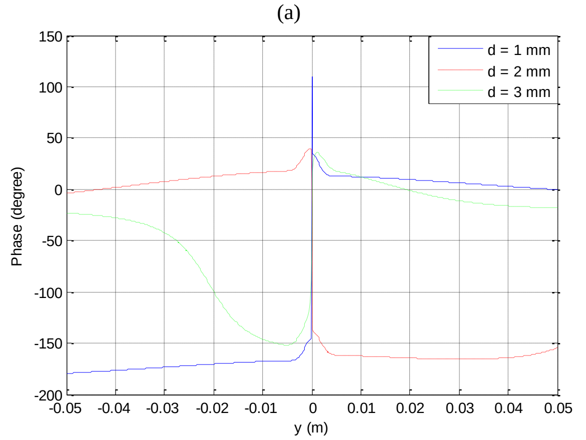

(b)

Figure 6: (a) Magnitude and (b) phase of crack signal ($H_{y,c}$) along the *y*-axis at a lift-off distance z_s = 0.7 mm below a rectangular inducer with *a* = 10 mm, *b* = 20 mm and *o′* = (0, 2 mm, 5 mm) in Figure 1, when the inducer is located in air and above steel half space containing a long hidden crack with gap distance *g* = 0.4 mm at different depths. For these plots, *f* = 1 kHz.

IV. CONCLUSION

A semi-analytical modeling technique was proposed to determine the magnetic field distributions due to an arbitrary-shape wire inducer around a hidden long crack in a ferrous metal. The modeling technique based on the waveguide theory hypothesizes a waveguide partially filled with a lossy dielectric, whose enclosure lies at infinity and the metal represents the lossy dielectric. The eigenvalue equation associated with TE modes in flawed region is changed to obtain convergent results. The mode-matching technique is used to solve the resultant boundary value problem. The accuracy of the proposed technique was confirmed by comparing the results with those obtained using the CST finite integration code. It has been found the proposed technique is computationally more efficient than the finite integration technique.

REFERENCES

[1] M. L. Burrows, "Theory Of Eddy-Current Flaw Detection", Dissertation, University of Michigan, 1964.

[2] J. R. Bowler, S. A. Jenkins, "Eddy-Current Probe Impedance Due To A Volumetric Flaw," *J. Appl. Phys*. vol. 70, pp. 1107-1114, 1991.

[3] Andrea Bernieri , Luigi Ferrigno, Marco Laracca, , "Eddy Current Testing Probe Based on Double-Coil Excitation and GMR Sensor," *IEEE Transactions on Instrumentation and Measurement*, vol. 68, Iss. 5, pp. 1533-1542, 2019.

[4] A. M. Lewis, D. H. Michael, M. C. Lugg, R. Collins, "Thin-Skin Electromagnetic Fields Around Surface Breaking Cracks In Metals," *J. Appl. Phys*. vol. 64, no. 6, pp. 3777-3784, 1988.

[5] S. H. H. Sadeghi, D. Mirshekar-Syahkal, "Scattering Of An Induced Field By Fatigue Cracks In Ferromagnetic Metals," *IEEE Trans. Magn*. vol. 28, no. 2, pp.1008-1016, 1992.

[6] D. Mirshekar-Syahkal, R. F. Mostafavi, "Analysis Technique For Interaction Of High-Frequency Rhombic Inducer Field With Cracks In Metals," *IEEE Trans. Magn*. vol. 33, no. 3, pp. 2291-2298, 1997.

[7] R. F. Mostafavi, D. Mirshekar-Syahkal, "AC Fileds Around Short Cracks In Metals Induced By Rectangular Inducers," *IEEE Trans. Magn*. vol. 35, no. 3, pp. 2001-2006, 1999.

[8] Z. Chen, G. Preda, O. Mihalach and K. Miya, "Reconstruction of Crack Shapes from the MFLT Signals by Using a Rapid Forward Solver and an Optimization Approach," *IEEE Trans. Magn*. vol. 38, no. 2, pp. 1025–1028, 2002.

[9] A. C. Okafor, S. Natarajan, "Multifrequency Eddy Current Inspection of Corrosion in Clad Aluminum Riveted Lap Joints and its Effect on Fatigue Life," *Review of Quantitative Nondestructive Evaluation*,vol. 26, pp.1274-1281, 2007.

[10] K. S. S. Rao, B. P. C. Rao, S. Thirunavukkarasu, "Development of Pulsed Eddy Current Instrument and Probe for Detection of Sub-Surface Flaws in Thick Materials," *IETE Technical Review*, vol. 34, no. 5, pp. 572-578, 2017.

[11] A. Sophian, G. Tian, M. Fan, "Pulsed Eddy Current Non-destructive Testing and Evaluation: A Review," *Chinese Journal of Mechanical Engineering*, vol. 30, no. 3, pp. 500–514, 2017.

[12] K. S. Rao, S. Mahadevan, B. P. C. Rao, S. Thirunavukkarasu, "A New Approach To Increase The Subsurface Flaw Detection Capability Of Pulsed Eddy Current Technique," Measurement: *Journal of the International Measurement Confederation*, vol. 128, pp. 516-526, 2018.

[13] Y. Li, T. Theodoulidis, G. Y. Tian, "Magnetic Field-Based Eddy-Current Modeling For Multilayered Specimens," *IEEE Trans. Magn*., vol. 43, no. 11, pp. 4010-4015, 2007.

[14] T. Theodoulidis, "Developments in Calculating The Transient Eddy-Current Response From A Conductive Plate," *IEEE Trans. Magn*., vol. 44, no. 7, pp. 1894-1896, 2008.

[15] W. Dehui, Y. Fan, W. Xiaohong, H. Tianfu, "Impedance Calculation Of Arbitrary-Shaped Thin-Walled Coils For Eddy-Current Testing Of Planar Media," *Sensors and Actuators A*, vol. 279, pp. 537–542, 2018.

[16] H. Sun, J. R. Bowler, T. P. Theodoulidis, "Eddy Currents Induced In A Finite Length Layered Rod By A Coaxial Coil," *IEEE Trans. Magn*. vol. 41, no. 9, pp. 2455- 2461, 2005.

[17] X. Chen, Y. Lei, "Time-Domain Analytical Solutions To Pulsed Eddy Current field Excited By A Probe Coil Outside A Conducting Ferromagnetic Pipe," *NDT&E International*, vol. 68, pp. 22–27, 2014.

[18] T. Theodoulidis, J. R. Bowler, "Impedance of a Coil at an Arbitrary Position and Orientation Inside a Conductive Borehole or Tube," *IEEE Trans. Magn*., vol. 51, no. 4, 2015.

[19] T. Theodoulidis, J. R. Bowler, "Eddy Current Interaction Of A Long Coil With A Slot In A Conductive Plate," *IEEE Trans. Magn*., vol. 41, no. 4, pp. 1238 – 1247, 2005.

[20] T. Theodoulidis, N. Poulakis, J. R. Bowler, "Developments in Modeling Eddy Current Interactions With A Right-Angled Conductive Wedge," *in Electromagnetic Nondestructive Evaluation (X)*, S. Takahashi and H. Kikuchi, Eds., IOS Press, pp. 41–48, 2007.

[21] T. Theodoulidis, J. R.Bowler, "Interaction of an Eddy-Current Coil With A Right-Angled Conductive Wedge," *IEEE Trans. Magn.,* vol. 46, no. 4, pp.1034-1042, 2010.

[22] C. P. Trampel, J. R. Bowler, "Eddy-Current Coil Interaction With A Perfectly Conducting Wedge Of Arbitrary Angle," *Research in Nondestructive Evaluation*, vol. 25, pp. 186–202, 2014.

[23] M. H. Ostovarzadeh,S. H. H.Sadeghi, R.Moini, "Field Distributions Around A Long Opening In A Metallic Half Space Excited By Arbitrary-Frequency Alternating Current-Carrying Wires Of Arbitrary Shape," *IEEE Trans. Magn.*, vol. 47, no. 11, pp. 4600-4610, 2011.

[24] M. H.Ostovarzadeh, S. H. H.Sadeghi, R.Moini, "Field Distribution Around A Long Crack In A Conductive Half Space Excited By An Arbitrary-Frequency Alternating-Current-Carrying Coil Of Arbitrary shape," *IET Sci. Meas. Technol.*, vol .6, no. 1, pp. 29–42, 2012.

[25] M. H.Ostovarzadeh, S. H. H.Sadeghi, R.Moini, "Field Distribution Around A Hidden Long Crack In A Conductive Half Space Excited By Arbitrary-Frequency Alternating-Current-Carrying Coil Of Arbitrary Shape," *NDT&E International*, vol. 48, pp. 54–62, 2012.

[26] M. H.Ostovarzadeh, "Analytical Solution For Interaction Of An Arbitrary Frequency Curved Rectangular Inducer With A Transverse Ring Shaped Groove Surrounding A Long Conductive Cylinder," *NDT and E International*, vol. 69, pp. 55-63, 2015.

[27] C. A. Balanis, *Advanced Engineering Electromagnetics*, John-Wiley & Sons, 1989.

[28] Computer Simulation Technology Software, http://www.cst.com. Accessed 22 November 2019.